Received: 6 January 2026 | Revised: 25 April 2026 | Accepted: 28 April 2026

DOI: 10.1111/jmi.70105

Journal of Microscopy RMS

METHODS AND PROTOCOLS

RNA-based CLEM (RCLEM) bridging RNA localisation and ultrastructural mapping in 3D

Daan Verhaege[1,2] | **Lore Van Acker**[1,2] | **Camille Wagner**[1,2] | **Yentl Van den Berghe**[1,3] | **Jérémy Verbeke**[1,4] | **Martin Guilliams**[1,2] | **Anna Kremer**[1,4] | **Lien Van Hoecke**[1,2] | **Roosmarijn E Vandenbroucke**[1,2]

[1]VIB-UGent Center for Inflammation Research, VIB, Ghent, Belgium

[2]Department of Biomedical Molecular Biology, Ghent University, Ghent, Belgium

[3]Department of Mathematics, Computer Science and Statistics, Ghent University, Ghent, Belgium

[4]VIB BioImaging Core, VIB, Ghent, Belgium

Correspondence
Roosmarijn E Vandenbroucke, VIB-UGent Center for Inflammation Research, VIB, Ghent, Belgium.
Email: Roosmarijn.Vandenbroucke@irc.vib-ugent.be

Funding information
Research Foundation-Flanders (FWO), Grant/Award Numbers: 3F017119, 1123625N, 1268823N, 3G055121; VIB Techwatch

Abstract

Spatial transcriptomics and in situ hybridisation techniques have become essential for contextualising single-cell RNA sequencing (scRNA-seq) data by mapping cell type– and state–specific mRNA expression within intact tissues. Beyond validating scRNA-seq predictions, these spatial methods provide critical insight into the localisation of specific cell types and their spatial relationships with neighbouring cells. However, current approaches rely on light microscopy (LM), which, despite advances, lacks the resolution needed to resolve detailed cell morphology or subcellular RNA localisation in situ. While correlative imaging methods can enhance spatial context, RNA detection remains limited by the optical constraints of LM. To overcome these challenges, we developed a three-dimensional RNA-based correlated light and electron microscopy (RCLEM) workflow. This method integrates RNA labelling with serial block-face scanning electron microscopy (SBF-SEM), allowing high-resolution 3D visualisation of RNA molecules within their ultrastructural environment. We optimised the RNA labelling protocol for thick, whole-mount tissues by fine-tuning detergent conditions to preserve ultrastructure while maintaining probe accessibility. This RCLEM approach offers several advantages over protein-based correlative methods, including robust detection with nucleotide probes and independence from antibody optimisation or fixation-sensitive epitopes. Applied to choroid plexus (ChP) and liver tissue, this workflow enabled precise 3D correlation between mRNA expression and EM features, supporting detailed morphological characterisation of rare scRNA-seq–defined cell subtypes. This protocol is broadly applicable to other complex tissues and provides a powerful platform for integrative, high-resolution spatial transcriptomic analyses that bridge gene expression with ultrastructure.

Daan Verhaege, Lore Van Acker, Anna Kremer, Lien Van Hoecke, and Roosmarijn E Vandenbroucke contributed equally to this work.

KEYWORDS
CLEM workflow, high-resolution confocal imaging, RCLEM, SBF-SEM

1 | INTRODUCTION

In recent decades, continuous advancements in microscopic visualisation have enabled the use of (super)resolution confocal imaging in light microscopy (LM) and volumetric three-dimensional (3D) visualisation via electron microscopy (EM).[1,2] Thanks to the improvements in LM, precise localisation of specific proteins and structures has increased;[3–5] especially with the advent of super-resolution confocal techniques, many subcellular structures can now be visualised. However, contextual information remains limited due to the inherent detection of only fluorescent labels and the still lower structural contrast and resolution compared to EM. Conversely, in EM, the development of volume-EM techniques for biological samples, such as serial block-face scanning EM (SBF-SEM) and focused ion beam SEM (FIB-SEM), allows for the acquisition of detailed ultrastructural information at nanometre resolution in 3D.[6,7] SBF-SEM incorporates a fully automated ultramicrotome within the EM vacuum chamber, facilitating the serial imaging and slicing of samples into sections as thin as 50 nm.[2,8,9] These 3D-EM datasets provide abundant contextual information, but specific protein or structure labelling and dynamic information remain challenging. To bridge this gap, 3D correlated light and electron microscopy (CLEM) was developed to combine LM and EM techniques.[10] 3D-CLEM images the same region of interest using both LM and EM, leveraging the strengths of both methods to offer contextual insights into fluorescent labels and and ultrastructural information.

While recent advances have enabled the combination of super-resolution and ultrastructural imaging, these approaches have largely been limited to protein markers. Applying similar methods to RNA markers for light microscopy (LM) visualisation has not been possible. Yet, RNA-focused techniques are becoming increasingly important: in situ hybridisation is now widely used not only to validate predictions from single-cell and single-nucleus RNA sequencing (scRNA-seq and snRNA-seq), but also to map cell locations and their spatial relationships within intact tissues. These spatial insights are critical, particularly since differences in RNA localisation, such as nuclear versus cytoplasmic distribution, may account for discrepancies between snRNA-seq and scRNA-seq datasets. For example, mRNAs are often still in the nucleus shortly after transcription, while translation occurs in the cytosol. Building on this, spatial transcriptomics technologies have recently emerged, enabling transcriptome-wide profiling of cells in their native tissue context. However, despite these advances, all of these RNA-based spatial methods still rely on conventional LM imaging, which lacks the resolution needed for detailed single-cell morphology and subcellular mRNA localisation.

Here, we bridge this gap by providing a workflow for RNA markers identified using scRNA-seq or snRNA-seq, while enabling EM morphological analysis of cell (sub)types of interest. The novelty of this workflow lies in the use of RNA markers in 3D-CLEM, making it possible to unravel cellular heterogeneity by examining mRNA marker expression in cells, tissue sections, and whole mount tissues integrated with ultrastructural information.

We optimised this workflow for two different tissue types, namely whole mount choroid plexus (ChP) and thick vibratome liver sections. The ChP is a small brain region important in producing the cerebrospinal fluid, maintaining brain homeostasis and the brain's response to inflammatory triggers.[11,12] It contains cuboidal epithelial cells ensheathing the vascular stroma, which consists of hard-to-distinguish cell types such as endothelial cells, fibroblasts, pericytes, and a vast array of myeloid cells. Localising different cell (sub)types and intercellular contacts, especially how these change upon disease, remains a challenge. Using SBF-SEM, we can easily identify epithelial cells and investigate their morphology. In contrast, pericytes, fibroblasts, endothelial, and immune cells, which are localised between the morphologically distinguishable epithelial layers, form a dense and tangled network, making it challenging to distinguish these cells from one another in a typical (3D) TEM/SEM image. Using scRNA-seq, it is possible to identify cell (sub)type-specific mRNA markers and, with fluorescent mRNA in situ hybridisation technologies, locate the 'rough' position of different cell (sub)types in the ChP. In addition to whole mounts of the ChP, we also optimised the RCLEM workflow for thick liver tissue sections. Kupffer cells, resident liver macrophages, and stellate cells, major players in liver fibrosis, have been successfully visualised via CLEM, demonstrating that Kupffer cells cross the endothelial cell barrier to contact stellate cells closely.[13] Deep scRNA-seq has revealed the presence of poorly studied stromal and myeloid cell subsets in the healthy liver and in situ RNA hybridisation experiments showed that these cells are located around the portal

veins.[13–15] While current imaging techniques, including high-resolution confocal microscopy, enable visualisation of many subcellular features, precise 3D ultrastructural localisation of these rare cell types within tissue context remains challenging. In addition, current mRNA staining and visualisation techniques are often limited in their ability to combine transcript detection with detailed morphological context, particularly at the (sub)cellular level in 3D tissue volumes. The typical dotted mRNA staining pattern combined with the dense cellular network found in the ChP and the portal vein area in the liver often obscures the identification of the cell to which the mRNA dots belong. To address this, we developed a workflow for RCLEM combining mRNA staining with morphological and (sub)cellular information obtained via SBF-SEM. Our technology complements upcoming spatial transcriptomics technologies, as RCLEM enables the investigation of the sub-cellular localisation of mRNA species.

2 | MATERIAL AND METHODS

2.1 | Animals

C57BL/6 mice were maintained in specific pathogen free (SPF) conditions in individually ventilated cages under a 10 h dark/14 h light cycle with free access to food and water. All animal studies were conducted in compliance with governmental and EU guidelines for the care and use of laboratory animals and were approved by the ethical committee of the Faculty of Sciences, Ghent University, Belgium (EC2022_004).

2.2 | Tissue preparation

To label blood vessels in the liver, mice were euthanised by gradual-fill carbon dioxide (CO_2) inhalation in accordance with institutional guidelines, and death was confirmed before further tissue processing. The inferior vena cava was cannulated for sequential perfusion with PBS containing 0.05 mM EDTA, followed by perfusion with 1/125 fluorescein isothiocyanate-labelled Concanavalin A (FITC-ConA; cat #FL-1001-25, VEC.FL-1001, Vector Laboratories), and finally with Antigenfix (cat #P0016, Diapath, Martinengo, Italy) at a flow rate of 5 mL/min for 5 min at room temperature (RT). For ChP samples, mice received an intravenous injection of 1 mg FITC-ConA. After 5 min, animals were anaesthetised with ketamine (100 mg/kg)/xylazine (20 mg/kg) and absence of reflexes was confirmed before tissue collection. Liver and ChP were collected and post-fixed in Antigenfix for 24 h at 4°C. The liver was further processed without embedding and cut into sections of 100 μm using a Leica Vibratome VT1200S (Leica; Nussloch, Germany) and the ChP tissue was further processed as whole mount.

2.3 | RNA staining

mRNA expression in 100 μm vibratome sections of liver and whole mount ChP tissue was detected using the RNAscope Multiplex Fluorescent v2 Assay (cat #323110, Advanced Cell Diagnostics, ACD), The manufacturer's protocol was adapted as described below. For liver, the RNAscope Cd5l probe (accession number: NM_009690.2; Biotechne) was assigned to channel C2 and detected with Opal-570 fluorophore (cat #FP1488001KT, Akoya Biosciences; 1:1000 dilution in TSA buffer). On ChP whole mounts, RNAscope Dpep1 (C1) probes (accession number: NM_007876.2; Biotechne) were used at 1:400 dilution, detected with Opal-650 (cat #FP1496001KT, Akoya Biosciences; at 1:1000 dilution). Liver samples were stained in 24-well plates using 200–400 μL of solution to fully cover the tissue, while ChP samples were stained in 96-well flat-bottom plates with 100–200 μL of solution. To exchange solutions during the protocol, the solution for liver samples was aspirated using a vacuum pump. In contrast, ChP samples were carefully transferred between wells using tweezers to avoid structural damage to the delicate tissue. Tissues were washed twice in PBS for 10 min at 4°C and incubated in PBS supplemented with 0.05% Tween (PBST) for 15 min at RT. Hydrogen peroxide (cat #322381, ACD) was applied for 10 min at RT, followed by three 5 min washes at RT in fresh PBS supplied with 0.05% TritonX100. Protease IV (cat #322381, ACD) was added until sections floated, and incubated for 30 min at 40°C. Sections were washed twice in distilled water before probe hybridisation for 2 h at 40°C. After hybridisation, sections were washed twice in 1× wash buffer at RT and stored overnight in 5× saline sodium citrate (SSC) at 4°C.

On the next day, sections were washed in 1× wash buffer and signal amplification was performed sequentially using AMP1, AMP2, and AMP3, each incubated for 30, 30, and 15 min at 40°C, with intermediate 5 min washes at RT. HRP-C1, HRP-C2, or HRP-C3 was then applied for 15 min at 40°C to develop the signal from Dpep1 or Cd5l respectively. After every HRP-C1/2/3 incubation, samples were washed for 5 min at RT in washing buffer. Corresponding Opal dyes were incubated for 30 min at 40°C, followed by 5 min washing at RT in washing buffer, and a 15 min incubation with HRP blocker (at 40°C, cat #323110, ACD) to prevent cross-reactivity. Finally, tissues were counterstained with DAPI (cat #323110, ACD). Liver sections were mounted in glycerol, and coverslips were sealed with nail polish. ChP whole mount samples were embedded in

2% agarose droplets large enough to contain the tissue, where placed in iBIDI imaging chambers and covered with glycerol to stay at the well bottom. All 40°C steps were performed in a humidity-controlled HybEZ oven (ACDbio).

The CLEM workflow used for these experiments is based on a workflow previously optimised for liver sections[10] and in short explained below.

2.4 | Near infrared branding

ChPs or liver sections were examined using a Zeiss LSM980-Airyscan2 confocal microscope (Carl Zeiss, Jena, Germany) for potential regions of interest (ROI). ROI were defined and were marked by near infrared branding (NIRB) with a Mai Tai®-AX HPDS DeepSee™ DC-36K laser (Spectra-Physics) coupled into the scan unit of the LSM980. For branding, an LD LCI Plan-Apochromat 25×/0.8 Imm Korr DIC M27 objective was used (pixel size 171 nm). The Mai Tai® laser was tuned to 750 nm and used at 50% power. Five cycles of 10 bleaching scans were performed at a pixel dwell time of 1.06 µs. Overview images were acquired with an LD LCI Plan-Apochromat 25×/0.8 Imm Korr DIC M27 objective in a 7 by 7 tile.

2.5 | High-resolution fluorescence light microscopy

High-resolution confocal stacks were obtained with a Zeiss LSM980-Airyscan2 confocal microscope (Carl Zeiss, Jena, Germany) in super-resolution Airyscan mode. Using a Plan-Apochromat 63×/1.40 Oil DIC M27 objective, a stack of on average 100 images was collected at a voxel size of 43 nm × 43 nm × 150 nm, using a 1.7× scan zoom, no tiles, resulting in a field of view of 78.21 × 78.21 µm. After this, the samples were prepared for EM, starting with overnight fixation in 2% paraformaldehyde (EMS) and 2.5% glutaraldehyde (EMS) in 0.1 M sodium cacodylate pH 7.4.

2.6 | Sample preparation for SBF-SEM

Free floating ChP tissue was embedded in 2% low-gelling temperature agarose (cat #A4018, Sigma-Aldrich; gelling temperature 26–30°C) before further processing for SBF-SEM. After overnight fixation at 4°C, samples were processed for volume-EM by performing en bloc heavy metal staining as described previously.[10,16] In short, samples were osmicated in 2% osmium (cat #50-332-11, Electron microscopy sciences, EMS), 1.5% ferricyanide in 0.1 M Sodium Cacodylate pH 7.4 for 1 h at RT. Osmium was removed by washing 5 times for 3 min in ultrapure water (UPW) and samples were immersed in 1% thiocarbohydrazide (20 min) at RT. After a second osmication in 2% osmium in UPW (30 min at RT), samples were washed and placed in uranyl acetate replacement stain (cat #22405, EMS) in water (1:3) overnight at 4°C. Samples were incubated in Walton's Lead (0.02 M Lead Nitrate in 0.03 M Aspartic Acid, with pH adjusted to 5.5 using 1 N KOH) at 65°C for 30 min. After the final washes, the samples were dehydrated using a series of solutions of increasing EtOH concentration (50%, 70%, 90%, 2 × 100%), followed by two dehydrations of 10 min in propylene oxide. Subsequent infiltration with EMBED-812 resin (cat #14121, EMS) was done by first incubating the samples for 2–4 h in 50% resin in propylene oxide, followed by an overnight incubation in 100% resin. The composition of EMBED-812 used was 10.8 g Embed812 (cat #14900, EMS), 7.4 g Dodecanyl Succinic Anhydride (DDSA. Specially Distilled, cat #13710, EMS), 4.5 g Methyl-5-Norbornene-2,3-dicarboxylic anhydride (NMA; cat #19000, EMS) and 0.54 g N-Benzyldimethylamide (BDMA; cat #11400-25, EMS).[17] The next day, after two more changes in fresh resin, the samples were flat-embedded between two microscopy slides in fresh resin and cured in the oven at 65°C for 72 h.

2.7 | SBF-SEM approach of the ROI and EM image acquisition

The resin-embedded samples were mounted on aluminium specimen pins (Melotte, Belgium) using conductive epoxy (CircuitWorks). Pins were placed in the Gatan 3View2XP (Gatan Inc, Milton UK) in a Zeiss Merlin SEM (Carl Zeiss, Oberkochen, Germany) for imaging at 1.6 kV with a Gatan Digiscan II ESB detector. First, ROIs were approached by removing 5–10 µm at increments of 100 nm. A reference image was taken after every 5 or 10 µm (50-100 sections) to check progress and see if NIRB marks were already visible. After locating the ROI, an imaging run was started with the software set to 1000 sections of 70 nm and image at 15 nm pixels.

2.8 | Combining LM and EM datasets

The resulting EM datasets were registered and converted to TIFF file format using IMOD (http://bio3d.colorado.edu/imod/) and the resulting TIFF-stacks were prepared for LM-EM overlays using Fiji (https://fiji.sc/). The LM data sets underwent post-acquisition Airyscan processing (pixel reassignment and 2D wiener deconvolution steps), followed by an additional joint deconvolution step to reach a (theoretical) resolution of 90×90 nm (Zeiss ZEN Blue 3.10

software). Overlays of confocal and volume-EM datasets were created using a landmark-based registration using the pattern of the blood vessels (BigWarp plugin in Fiji[18]).

In case of limited volumetric overlap between LM and EM modalities and challenging identification of corresponding regions, a global alignment was first defined by calculating an affine transformation based on the graph representations of the blood vessel patterns.

3 | RESULTS

3.1 | Optimisation of RNA staining and LM-detection for EM compatibility

One of the main challenges in combining light microscopy (LM) and electron microscopy (EM) is finding a sample preparation protocol that meets the requirements of both imaging modalities. For effective intracellular fluorescent labelling, tissue samples typically need to be permeabilised using detergents to ensure adequate penetration of dyes and washing buffers. However, this permeabilisation step can severely compromise cell membranes and overall tissue morphology, which are critical for high-quality EM imaging.

To address this, a balance must be struck: LM staining must be performed under milder detergent conditions to preserve the ultrastructural integrity needed for EM. Unlike protein detection, which relies on large antibody-based probes, mRNA detection benefits from small nucleotide-based amplification systems. This allows for reduced detergent concentrations during permeabilisation, minimising ultra-structural damage and making it more compatible with EM imaging.

In this study, we optimised RNAScope in situ hybridisation staining protocols for thick liver tissue sections and whole-mount choroid plexus (ChP) samples, ensuring compatibility with subsequent EM preparation and imaging. In ChP, we targeted *Dpep1*, a transcript enriched in a fibroblast population identified through scRNA-seq.[19] These *Dpep1*-positive fibroblasts are located near capillaries, but their precise microenvironment is difficult to resolve using LM alone. In the liver, we focused on *Cd5l*, an mRNA marker that specifically identifies Kupffer cells across species.[20]

We systematically tested a variety of conditions to develop a protocol compatible with both LM and EM. This included adjusting the compositions of, for example, hybridisation and amplification buffers, evaluating treatments with ethanol, paraformaldehyde, and proteases. We ultimately decided to completely omit ethanol-based dehydration steps to better preserve ultrastructure. A crucial part of the process was replacing standard RNA labelling detergents with milder alternatives that still provided strong mRNA signals for LM. During initial protocol development using Molecular Instruments mRNA staining, we extensively optimised permeabilisation conditions by testing different detergents and concentrations during washing, hybridisation, and amplification steps. Washing buffers contained PBS supplemented with 0.01%–0.05% saponin or 0.1% Tween-20, while hybridisation and amplification buffers were tested with 0.005%–0.05% saponin, 0.1% Triton X-100, or 0.1% Tween-20 (Figure S1). In addition, we tested different concentrations of glutaraldehyde in the fixative to improve tissue preservation. Although these conditions produced detectable signal, they did not provide an optimal balance between RNA detection efficiency and ultrastructural preservation. We therefore transitioned to the RNAscope platform (ACD) and further simplified the protocol. In the final workflow, detergent exposure was minimised and limited to a brief 0.05% PBSTween-20 wash during the initial steps, while saponin and glutaraldehyde were omitted because of their negative effects on ultrastructural preservation and RNA staining, respectively.

Representative mRNA staining images for *Dpep1* in ChP and *Cd5l* in liver tissue are shown in Figure 1A and B, respectively. Similarly treated samples were also further processed for EM to check the quality of the ultrastructure. Figure 1C–F shows that for both ChP and liver tissue ultra-structure was of high enough quality in case of the final protocol.

3.2 | Workflow for precise correlation between LM and EM

Fiducial markers are essential for accurate navigation between LM and EM, as well as for precise correlation of LM and EM datasets during imaging and data analysis. In this study, we adapted a previously published workflow that successfully combined near infrared branding (NIRB) with blood vessel labelling in the liver to perform protein-CLEM.[13] NIRB is a technique where a 2-photon laser is applied at high energy to destroy a focused area in a tissue sample.[21] Branding conditions were optimised to produce distinct, localised marks without damaging adjacent tissue. As previously described,[13] the samples were imaged in LM and an ROI was determined. Once the position was found, 3 branding marks were made in the shape of an arrow (Figure 2A). Subsequently, a high-resolution z-stack of the ROI was taken including the cell of interest and the end of the branding marks (Figure 2B). This helps with orientation of the datasets in the initial steps of data processing. At this point, the samples were removed from the microscope slide, fixed for EM and dissected

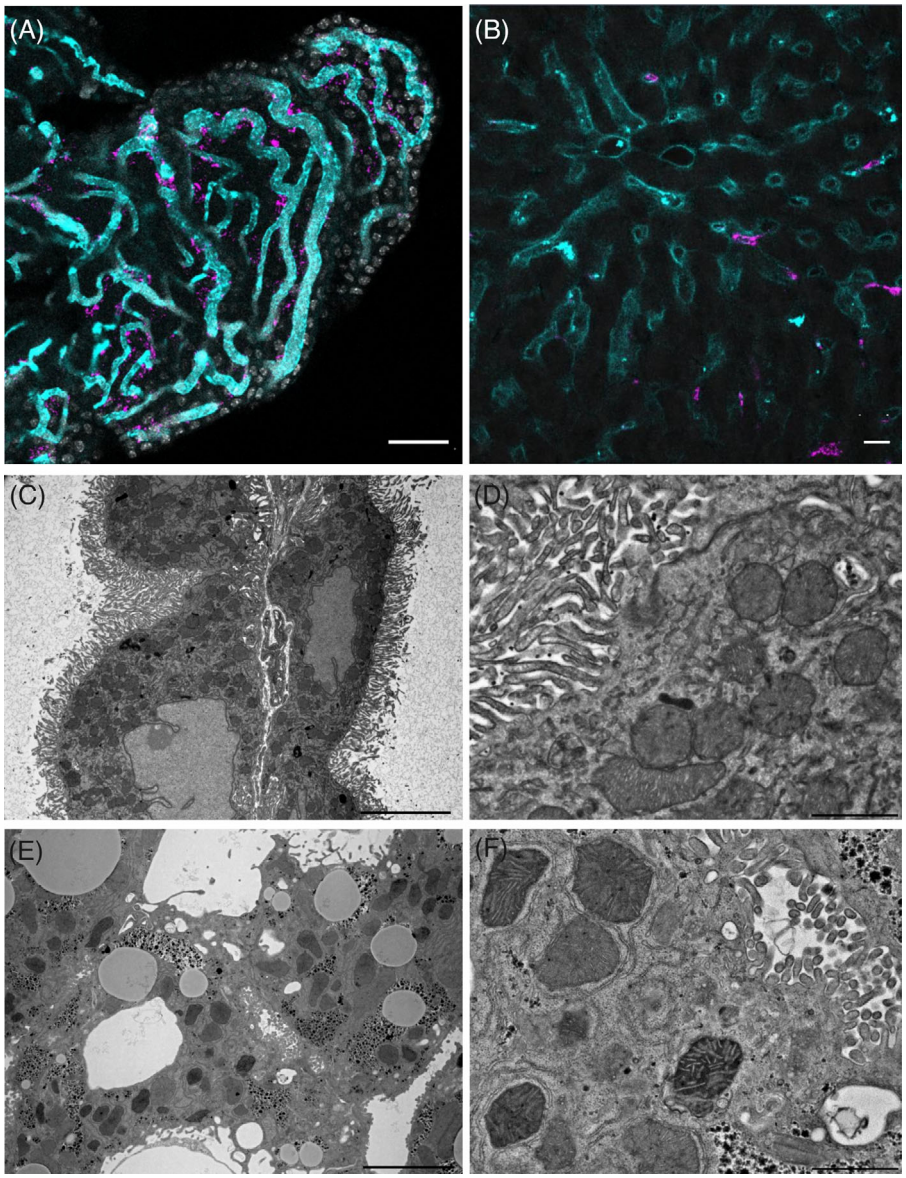

FIGURE 1 Representative images of RNA staining and underlying ultra-structure. (A, B) Representative LM images of ChP tissue (A) and liver tissues (B), with ConA-FITC (cyan), *Dpep1* or *Cd5l* (magenta) and DAPI (white). Scale bar: 50 μm (A). (C, D) Representative TEM images of ChP tissue that was processed with the optimised protocol for RNA staining, showing the intact cellular ultrastructure (C) as well as nice microvilli and mitochondrial cristae (D). Scale bars: 5 μm (C) and 1 μm (D). (E, F) Representative TEM images of liver tissue that were processed for RNA staining. As for the ChP, also in liver, mitochondrial cristae are intact (E) and the overall structure of the tissue is maintained (F). Scale bars: 4 μm (E) and 1 μm (F).

into a smaller piece (Figure 2C and D), encompassing the ROI and the branding marks. The tissue was intentionally trimmed asymmetrically to ensure correct orientation could be maintained, even after EM processing rendered the sample fully opaque. Once processed and embedded in resin, the sample was dissected into an even smaller piece (Figure 2D, red box), which was mounted on an aluminium pin for SBF-SEM (Figure 2E). Of note, the tissue was mounted perpendicular to the confocal Z-stack planes as described.[13]

Once in the SBF-SEM, the surface of the block was scanned for branding marks. In case none were present at the surface yet, sectioning commenced, and the surface was checked for the presence of branding marks every 5–10 μm. In ChP, the branding marks were clearly visible (Figure 2F), while in liver tissue the marks are harder to distinguish due to the abundance of blood vessels in the tissue (Figure 2G). However, in both tissues branding marks were found consistently and could be followed down to the ROI.

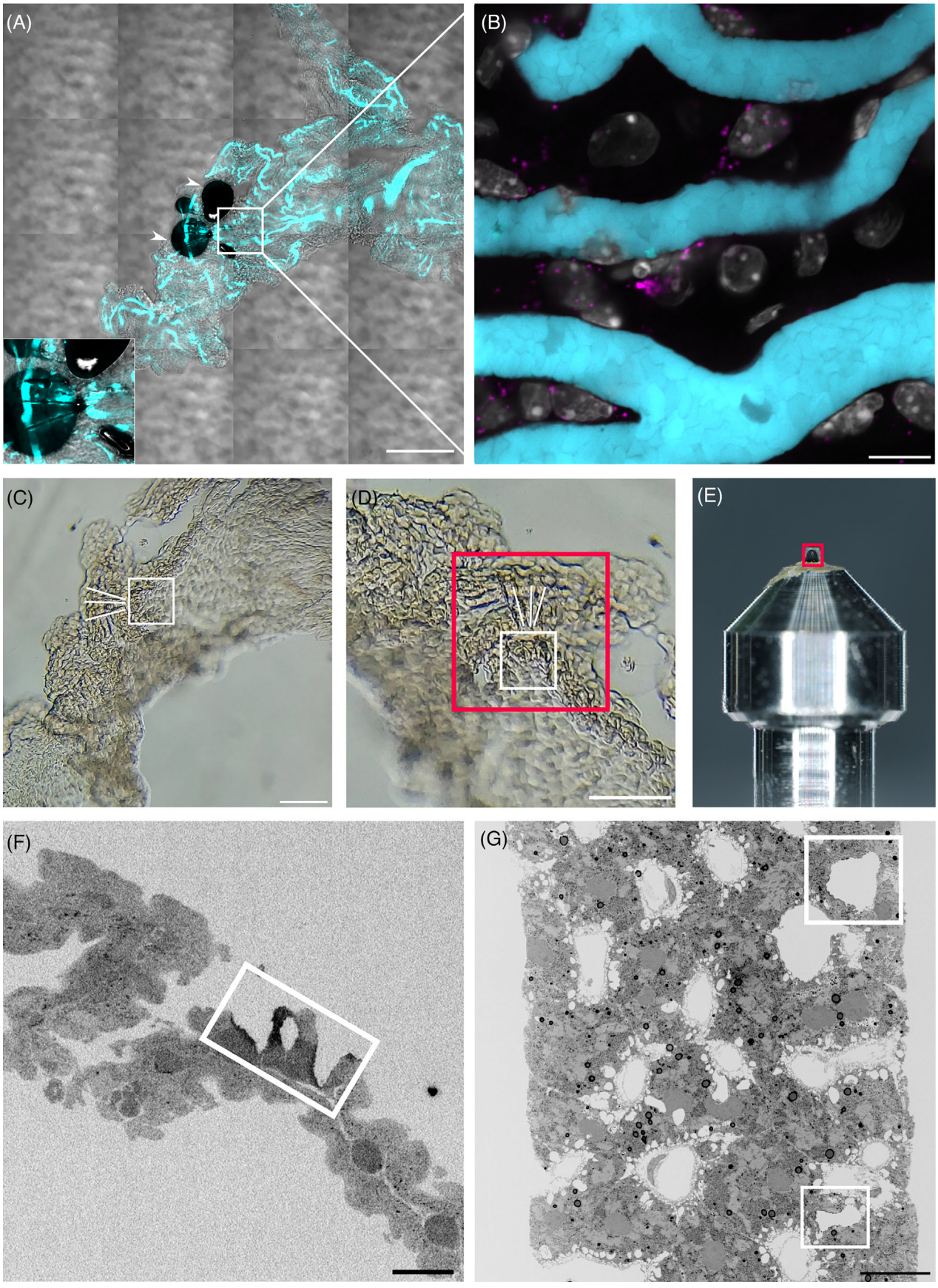
(A)
(B)
(C)
(D)
(E)
(F)
(G)

3.3 | Automated dataset alignment for integrated LM-EM analysis

After collecting the SBF-SEM data, the EM data was registered and resliced as described.[10] During this step, the position of the branding marks was used to match the orientation of the EM dataset to the LM data. Next, the blood vessel network, visible in both modalities and independent of the RNA of interest, was used as a fiducial marker to align the LM and EM datasets markers. However, because the samples were mounted manually, the SBF-SEM datasets did not always align perfectly with the confocal z-stacks. As a result, the datasets sometimes only partially overlapped, making it difficult to directly match the blood vessels between LM and EM. To overcome this, an in-house automated global alignment algorithm was applied as recently published.[22] This method converts the blood vessel patterns into graph representations. From these graphs, it generates candidate affine transformation matrices, ensuring they reflect biologically realistic shear and scale values. Each candidate transformation was applied to LM volume, and the resulting overlays with the EM data is evaluated using mutual information as a measure of similarity. The transformation with the highest mutual information score is selected as the best global alignment, which serves as the starting point for further local refinement.

The initial low-resolution overlay, based on the blood vessel graphs, helped to identify the overlapping regions between the datasets. This made it easier to locate landmarks that could be used for creating more precise overlays. For these landmarks, we used blood vessel staining in all cases, and for the ChP datasets specifically, we also used DAPI staining. The distinct shape of the nuclei made them easy to recognise in both imaging modalities. Using this, we were able to achieve precise overlays of LM and EM data of both ChP (Figure 3A–C; Video S1) and liver tissue (Figure 3D–F; Video S2). In the ChP, *Dpep1*-positive fibroblasts were clearly seen in close contact with capillaries (Figure 3A–C), allowing detailed structural analysis. In the liver, *Cd5l*-positive Kupffer cells were readily identified (Figure 3D–F).

After the initial overlay of the complete datasets, we created a more detailed overlay by focusing on a cropped region from a higher-resolution version of the SBF-SEM dataset. For the ChP, this detailed view confirmed the findings from the LM data: most of the RNA-positive puncta (Figure 3G) are located outside the nucleus. In addition, the nuclei of the *Dpep1*-positive fibroblasts appeared slightly darker than those of the surrounding choroid plexus endothelial cells. The same was done for a liver dataset (Figure 3H) showing the *Cd5l*-signal clearly only in the Kupfer cell and its long projections.

4 | DISCUSSION

In this study, we present a novel RNA-based correlated light and electron microscopy (RCLEM) workflow that enables spatial and subcellular visualisation of mRNA in complex tissues. This approach bridges the gap between transcriptomic labelling and three-dimensional ultrastructural imaging, extending the capabilities of traditional CLEM methods beyond protein detection. The protocol integrates optimised tissue preparation, mRNA staining, high-resolution fluorescence imaging, near-infrared branding (NIRB), and serial block-face electron microscopy (SBF-SEM). Throughout the workflow, we carefully balanced the requirements of fluorescence-based mRNA detection with the preservation of fine ultrastructural detail required for EM imaging.

We applied this method to whole-mount choroid plexus (ChP) tissue and thick liver sections, two challenging tissue types with high cellular density and structural complexity. Alignment between LM and EM datasets was achieved using vascular landmarks and NIRB fiducial marks that are detectable in both imaging modalities. While NIRB has previously been used for protein-CLEM in liver[13] and ChP[19] tissue, we successfully adapted this approach to enable accurate correlative imaging of RNA in both the ChP and liver,

FIGURE 2 Determination of ROI and NIRB in LM. (A) An overview image of a CP sample in brightfield, showing the fluorescent signal in the blood vessels (Cyan) and the ROI (white box). The branding marks are covered by air-bubbles caused by the near infrared branding (white arrowhead) and are shown in more detail in the inset in the left bottom corner. Scale bar 200 μm. (B) Maximum projection image of the high-resolution Z-stack of the ROI showing the blood vessels in cyan, the RNA staining in magenta and DAPI in white. Scale bar 10 μm. (C) Overview image of the tissue after LM imaging showing the branding marks (white lines) and ROI (white box). A small piece is dissected (shown in D by cropping) from the whole-mount to be used for EM processing. Scale bar 100 μm. (D) Area of the tissue that was processed for EM showing region (red box) that was mounted for SBF-SEM. This region includes the ROI and branding marks (white lines & box). Scale bar 100 μm. (E) Picture of aluminium pin for SBF-SEM sample with the final block mounted 90° turned with respect to the confocal Z-stack images. Inside the block, the branding marks are at the top, positioned as shown in D. (F) An image of ChP showing the 3 branding marks after approaching (white box). Scale bar 20 μm. (G) A similar image of liver tissue, also showing 2 of the 3 branding marks (white box at top and bottom right). Scale bar 20 μm.

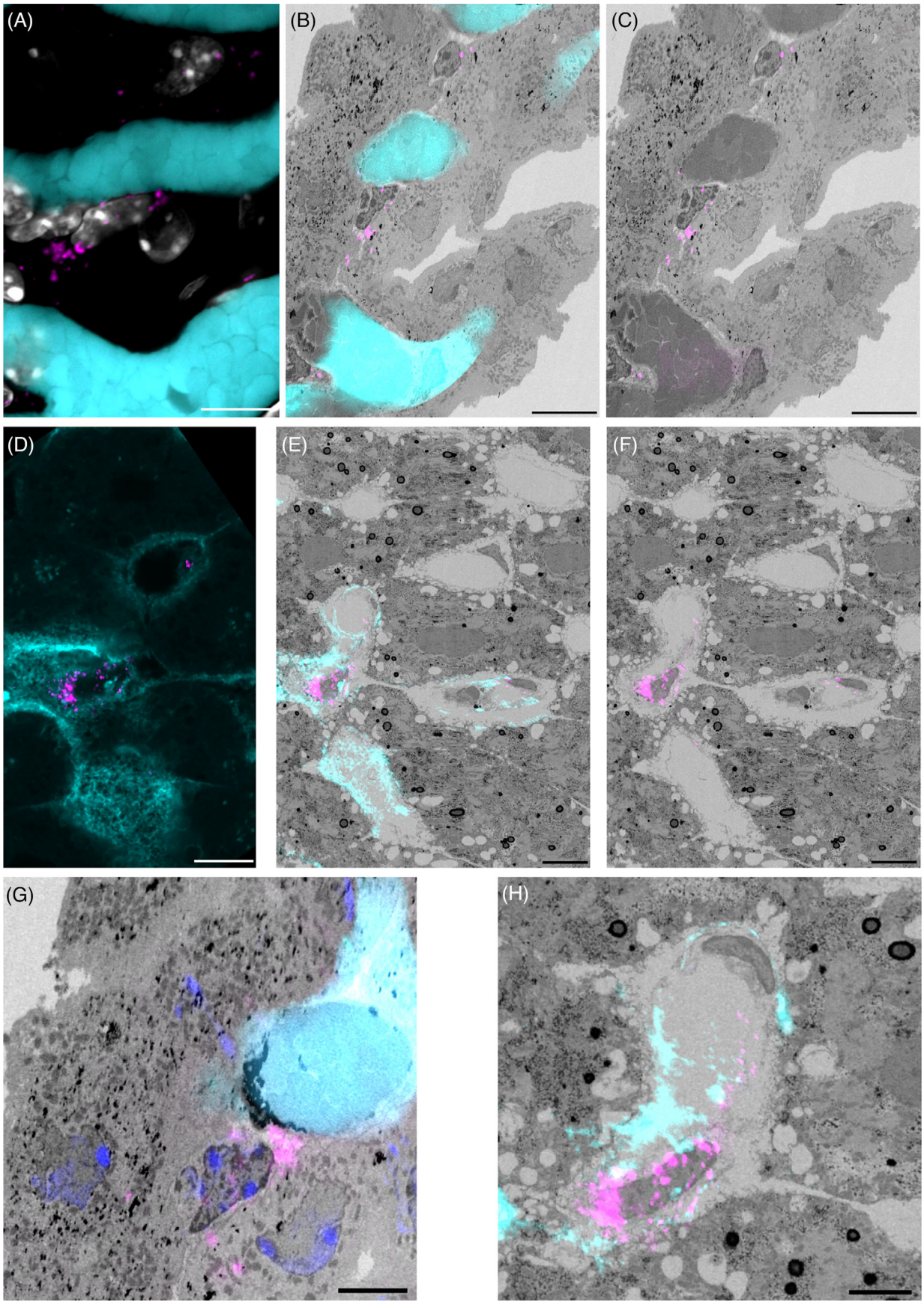
(A)
(B)
(C)
(D)
(E)
(F)
(G)
(H)

demonstrating the flexibility and robustness of the workflow.

Our method provides several key technical advantages over existing CLEM and current RNA detection protocols. Most notably, it supports mRNA staining under mild permeabilisation conditions, preserving membrane integrity and tissue morphology essential for EM. In contrast to antibody-based protein detection, which often requires harsh treatments and bulky probes, mRNA detection relies on small nucleotide-based hybridisation and amplification systems. This enables efficient staining in thick tissue samples without sacrificing EM quality, making the protocol highly adaptable and less reliant on target-specific optimisation steps. Additionally, unlike protein markers that may be compromised by fixation-induced epitope loss, mRNA targets remain accessible and intact, ensuring reliable detection. This makes mRNA staining a more robust and consistent strategy for correlative imaging workflows. Compared to current spatial transcriptomics platforms, which offer broad transcriptome coverage but limited spatial resolution, RCLEM can provide subcellular localisation of specific mRNA species within their precise structural context. This is particularly valuable for investigating rare or spatially restricted cell populations. In the ChP, we were able to visualise *Dpep1*-positive fibroblasts in direct association with capillaries, confirming predictions made by scRNA-seq[19] and adding structural resolution that LM alone could not provide. Similarly, *Cd5l*-positive Kupffer cells in the liver were identified within the sinusoidal niche, enabling detailed characterisation of their microenvironment and potential interactions with neighbouring cells.

Despite these strengths, our approach also comes with limitations. A key constraint is the trade-off between resolution and throughput: while RCLEM offers nanometre-scale detail, it is currently limited to small volumes and low multiplexing capacity. Tissue distortion during processing and partial fluorescence quenching during EM preparation can affect alignment precision and signal quality, posing challenges for quantitative interpretation. Nonetheless, by leveraging the compact size of RNA probes and mild processing conditions, we minimised these effects and demonstrated the feasibility of subcellular RNA localisation in structurally intact tissues.

The versatility of the RCLEM workflow offers exciting opportunities for future applications. It could be extended to disease models such as neuroinflammation or liver fibrosis, where understanding the cellular microenvironment and gene expression at high resolution is crucial. Incorporating multiplexed RNA detection would allow simultaneous mapping of multiple transcripts, while future integration with protein-based CLEM could enable comprehensive, multimodal analyses of gene and protein expression within their structural context. Additionally, the method could be adapted to study dynamic RNA processes, such as localisation during translation or stress responses. The optimised RCLEM technology also has potential to give us a better understanding of the localisation of mRNA within a cell, i.e. the nucleus or cytoplasm of a cell. In this way, it could help clarify discrepancies sometimes observed between single-cell and single-nucleus sequencing approaches.

From a more technical point of view, the precision of the overlay could be improved by using array tomography (AT)[23] instead of SBF-SEM. As SBF-SEM is an inherently destructive method, we must balance resolution with the aim to include the complete ROI in an imaging run. Switching to AT, where the sectioning happens outside of the microscope and ribbons of sections are imaged, a large overview can be combined with higher resolution imaging of specific ROIs.[24]

In conclusion, the RCLEM workflow introduced here addresses a significant gap in spatial biology by enabling subcellular mRNA localisation within a detailed 3D ultrastructural framework. It serves both as a technical blueprint and a biological tool, especially useful for validating scRNA-seq predictions and investigating rare or poorly characterised cell types. By combining RNA-based labelling with high-resolution EM, our method bridges the limitations of current spatial transcriptomics and protein-CLEM approaches. It provides a powerful and generalisable platform for future studies requiring precise correlation between transcript localisation and cellular architecture.

FIGURE 3 Overlay of fluorescence on SBF-SEM datasets. (A) Confocal z-slice of a ChP dataset showing the blood vessels (cyan) filled with red blood cells, DAPI (white) and *DpepI* signal (magenta). Scale bar 10 μm. (B) Confocal data overlayed onto the SBF-SEM data showing the same region as in A. Scale bar 10 μm. (C) Similar image as displayed in B without the fluorescent blood vessel staining to show the underlying SBF-SEM image. Scale bar 10 μm. (D) Confocal z-slice of a liver dataset showing the blood vessels (cyan) and the *Cd5l* signal (magenta). Liver tissue was perfused, hence the absence of red blood cells. Scale bar 10 μm. (E) An overlayed image of the confocal and SBF-SEM data of the same region as in D. (F) The overlay image without the fluorescent blood vessel staining. Scale bar 10 μm. (G) Cropped areas of a ChP dataset where the overlay was made with a higher resolution version of the SBF-SEM data. Note the *DpepI* signal (magenta) surrounding the nucleus (DAPI, dark blue). Scale bar: 4 μm. (H) A similar higher resolution overlay of a liver dataset. Scale bar 4 μm.

ACKNOWLEDGEMENTS

This work was supported by Research Foundation-Flanders (FWO) (3F017119, 1123625N, 1268823N, 3G055121) and VIB Techwatch.

ORCID

Yentl Van den Berghe https://orcid.org/0000-0002-4893-6225

Anna Kremer https://orcid.org/0000-0002-4613-1060

REFERENCES

1. Peddie, C. J., & Collinson, L. M. (2014). Exploring the third dimension: Volume electron microscopy comes of age. *Micron*, *61*, 9–19. https://doi.org/10.1016/j.micron.2014.01.009
2. Kremer, A., Lippens, S., Bartunkova, S., Asselbergh, B., Blanpain, C., Fendrych, M., Goossens, A., Holt, M., Janssens, S., Krols, M., Larsimont, J., Mc Guire, C., Nowack, M., Saelens, X., Schertel, A., Schepens, B., Slezak, M., Timmerman, V., Theunis, C., … Guérin, C. (2015). Developing 3D SEM in a broad biological context. *Journal De Microscopie*, *259*, 80–96. https://doi.org/10.1111/jmi.12211
3. Garini, Y., Vermolen, B. J., & Young, I. T. (2005). From micro to nano: Recent advances in high-resolution microscopy. *Current Opinion in Biotechnology*, *16*, 3–12. https://doi.org/10.1016/j.copbio.2005.01.003
4. Heintzmann, R., & Ficz, G. (2013). Breaking the resolution limit in light microscopy. *Methods in Cell Biology*, *114*, 525–544. https://doi.org/10.1016/B978-0-12-407761-4.00022-1
5. Heintzmann, R., & Ficz, G. (2006). Breaking the resolution limit in light microscopy. *Briefings in Functional Genomics & Proteomics*, *5*, 289–301. https://doi.org/10.1093/bfgp/ell036
6. Denk, W., & Horstmann, H. (2004). Serial block-face scanning electron microscopy to reconstruct three-dimensional tissue nanostructure. *PLOS Biology*, *2*, e329. https://doi.org/10.1371/journal.pbio.0020329
7. Heymann, J. A., Hayles, M., Gestmann, I., Giannuzzi, L. A., Lich, B., & Subramaniam, S. (2006). Site-specific 3D imaging of cells and tissues with a dual beam microscope. *Journal of Structural Biology*, *155*, 63–73. https://doi.org/10.1016/j.jsb.2006.03.006
8. Smith, D., & Starborg, T. (2019). Serial block face scanning electron microscopy in cell biology: Applications and technology. *Tissue & Cell*, *57*, 111–122. https://doi.org/10.1016/j.tice.2018.08.011
9. Lippens, S., Kremer, A., Borghgraef, P., & Guérin, C. J. (2019). Serial block face-scanning electron microscopy for volume electron microscopy. *Methods in Cell Biology*, *152*, 69–85. https://doi.org/10.1016/bs.mcb.2019.04.002
10. Kremer, A., Van Hamme, E., Bonnardel, J., Borghgraef, P., Guérin, C., Guilliams, M., & Lippens, S. (2021). A workflow for 3D-CLEM investigating liver tissue. *Journal De Microscopie*, *281*, 231–242. https://doi.org/10.1111/jmi.12967
11. Xu, H., Lotfy, P., Gelb, S., Pragana, A., Hehnly, C., Byer, L. I., Shipley, F. B., Zawadzki, M. E., Cui, J., Deng, L., Taylor, M., Webb, M., Lidov, H. G., Andermann, M. L., Chiu, I. M., Ordovas-Montanes, J., & Lehtinen, M. K. (2024). The choroid plexus synergizes with immune cells during neuroinflammation. *Cell*, *187*, 4946–4963. e4917. https://doi.org/10.1016/j.cell.2024.07.002
12. Baruch, K., Deczkowska, A., David, E., Castellano, J. M., Miller, O., Kertser, A., Berkutzki, T., Barnett-Itzhaki, Z., Bezalel, D., Wyss-Coray, T., Amit, I., & Schwartz, M. (2014). Aging. Aging-induced type I interferon response at the choroid plexus negatively affects brain function. *Science*, *346*, 89–93. https://doi.org/10.1126/science.1252945
13. Bonnardel, J., T'Jonck, W., Gaublomme, D., Browaeys, R., Scott, C. L., Martens, L., Vanneste, B., De Prijck, S., Nedospasov, S. A., Kremer, A., Van Hamme, E., Borghgraef, P., Toussaint, W., De Bleser, P., Mannaerts, I., Beschin, A., van Grunsven, L. A., Lambrecht, B. N., Taghon, T., … Guilliams, M. (2019). Stellate cells, hepatocytes, and endothelial cells imprint the Kupffer cell identity on monocytes colonizing the liver macrophage niche. *Immunity*, *51*, 638–654. e639. https://doi.org/10.1016/j.immuni.2019.08.017
14. Payen, V. L., Lavergne, A., Alevra Sarika, N., Colonval, M., Karim, L., Deckers, M., Najimi, M., Coppieters, W., Charloteaux, B., Sokal, E. M., & El Taghdouini, A. (2021). Single-cell RNA sequencing of human liver reveals hepatic stellate cell heterogeneity. *JHEP Reports: Innovation in Hepatology*, *3*, 100278. https://doi.org/10.1016/j.jhepr.2021.100278
15. MacParland, S. A., Liu, J. C., Ma, X., Innes, B. T., Bartczak, A. M., Gage, B. K., Manuel, J., Khuu, N., Echeverri, J., Linares, I., Gupta, R., Cheng, M. L., Liu, L. Y., Camat, D., Chung, S. W., Seliga, R. K., Shao, Z., Lee, E., Ogawa, S., … McGilvray, I. D. (2018). Single cell RNA sequencing of human liver reveals distinct intrahepatic macrophage populations. *Nature Communications*, *9*, 4383. https://doi.org/10.1038/s41467-018-06318-7
16. Deerinck, T. J., Bushong, E. A., Ellisman, M. H., & Thor, A. (2022). Preparation of biological tissues for serial block face scanning electron microscopy (SBEM) V.2. https://doi.org/10.17504/protocols.io.36wgq7je5vk5/2
17. Borghgraef, P., Kremer, A., De Bruyne, M., Guerin, C. J., & Lippens, S. (2023). Resin comparison for serial block face scanning volume electron microscopy. *Methods in Cell Biology*, *177*, 33–54. https://doi.org/10.1016/bs.mcb.2023.01.011
18. Bogovic, J. A., H, P., Wong, A., & Saalfeld, S., in *2016 IEEE 13th International Symposium on Biomedical Imaging (ISBI)* (2016).
19. Verhaege, D., xsDe Nolf, C., Van Acker, L., Claeys, W., Castelein, J., Van Wonterghem, E., Van Imschoot, G., Dujardin, P., De Spiegelaere, W., Hoste, E., Boone, F., Lidov, H. G. W., Dani, N., Derk, J., Kremer, A., Van Hamme, E., Borghgraef, P., Lippens, S., Lehtinen, M. K., … Vandenbroucke, R. E. (2026). Base barrier cells provide compartmentalization of choroid plexus, brain and CSF. *Nature Neuroscience*, *29*(3), 551–566. https://doi.org/10.1038/s41593-025-02188-7
20. Guilliams, M., Bonnardel, J., Haest, B., Vanderborght, B., Wagner, C., Remmerie, A., Bujko, A., Martens, L., Thoné, T., Browaeys, R., De Ponti, F. F., Vanneste, B., Zwicker, C., Svedberg, F. R., Vanhalewyn, T., Gonçalves, A., Lippens, S., Devriendt, B., Cox, E., … Scott, C. L. (2022). Spatial proteogenomics reveals distinct and evolutionarily conserved hepatic macrophage niches. *Cell*, *185*, 379–396. e338. https://doi.org/10.1016/j.cell.2021.12.018

21. Bishop, D., Nikić, I., Brinkoetter, M., Knecht, S., Potz, S., Kerschensteiner, M., & Misgeld, T. (2011). Near-infrared branding efficiently correlates light and electron microscopy. *Nature Methods*, *8*, 568–570. https://doi.org/10.1038/nmeth.1622
22. Van den Berghe, Y., Kremer, A., Verhaege, D., Vandenbroucke, R., & Saeys, Y. (2025). Corelative light and electron microscopy (CLEM) image registration by blood vessel axes alignment. BioRxiv. https://doi.org/10.1101/2025.06.23.661033
23. Micheva, K. D., & Smith, S. J. (2007). Array tomography: A new tool for imaging the molecular architecture and ultrastructure of neural circuits. *Neuron*, *55*, 25–36. https://doi.org/10.1016/j.neuron.2007.06.014
24. White, I. J., & Burden, J. J. (2023). A practical guide to starting SEM array tomography – An accessible volume EM technique. *Methods in Cell Biology*, *177*, 171–196. https://doi.org/10.1016/bs.mcb.2022.12.023

SUPPORTING INFORMATION

Additional supporting information can be found online in the Supporting Information section at the end of this article.

How to cite this article: Verhaege, D., Van Acker, L., Wagner, C., Van den Berghe, Y., Verbeke, J., Guilliams, M., Kremer, A., Van Hoecke, L., & Vandenbroucke, R. E. (2026). RNA-based CLEM (RCLEM) bridging RNA localisation and ultrastructural mapping in 3D. *Journal of Microscopy*, *303*, 120–131. https://doi.org/10.1111/jmi.70105